

Unveiling dynamic bifurcation of Resch-patterned origami for self-adaptive impact mitigation structure

Yasuhiro Miyazawa,^{1,2} Chia-Yung Chang,¹ Qixun Li,¹ Ryan Tenu Ahn,³
Koshiro Yamaguchi,^{1,2} Seonghyun Kim,² Minho Cha,² Junseo Kim,² Yuyang
Song,⁴ Shinnosuke Shimokawa,⁴ Umesh Gandhi,⁴ and Jinkyu Yang^{2,*}

¹*Department of Aeronautics and Astronautics,
University of Washington, Seattle, Washington 98195-2400, USA*

²*Department of Mechanical Engineering,
Seoul National University, 1 Gwanak-ro,
Gwanak-gu, Seoul 08826, South Korea*

³*Department of Chemistry, University of Washington,
Seattle, Washington 98195-2400, USA*

⁴*Toyota Research Institute North America,
1555 Woodridge Ave, Ann Arbor, Michigan 48105, USA*

(Dated: April 24, 2024)

Abstract

In the classic realm of impact mitigation, targeting different impact scenarios with a universally designed device still remains an unassailable challenge. In this study, we delve into the untapped potential of Resch-patterned origami for impact mitigation, specifically considering the adaptively reconfigurable nature of the Resch origami structure. Our unit-cell-level analyses reveal two distinctive modes of deformation, each characterized by contrasting mechanical responses: the folding mode that displays monostability coupled with strain-hardening, and the unfolding mode that manifests bistability, facilitating energy absorption through snap-through dynamics. Drop tests further unveil a novel dynamic bifurcation phenomenon, where the origami switches between folding and unfolding depending on impact speed, thereby showcasing its innate self-reconfigurability in a wide range of dynamic events. The tessellated meter-scale Resch structure mimicking an automotive bumper inherits this dynamically bifurcating behavior, demonstrating the instantaneous morphing into favorable deformation mode to minimize the peak acceleration upon impact. This suggests a self-adaptive and universally applicable impact-absorbing nature of the Resch-patterned origami system. We believe that our findings pave the way for developing smart, origami-inspired impact mitigation devices capable of real-time response and adaptation to external stimuli, offering insights into designing universally protective structures with enhanced performance in response to various impact scenarios.

I. INTRODUCTION

Impact mitigation remains an enduring challenge across diverse disciplines, including automotive, aerospace, sports science, and biomedicine. Traditional materials and structures, such as foam materials, damper systems, and crashworthy frames, have been used widely, each of which targets specific impact conditions and corresponding energy absorption mechanisms. However, due to the wide-ranging impact conditions, such as low-speed pedestrian impact to high-speed head-to-head collision of automotive vehicles, concussion-causing mild impact to a crash of sports and motorcycle helmets, and low- to high-speed ballistic impact in aerospace applications, it has always been a challenge to develop an omnifarious material

* jkyang11@snu.ac.kr

or structure that caters to different scenarios of energy absorption. For instance, in low-speed collisions, the soft and elastic medium is typically preferred for absorbing energy efficiently but is not suitable for high-speed and momentum impact scenarios. On the other front, the stiff and multi-stable (typically plastic) materials are considered ideal for the high-speed impact case, which is clearly the opposite requirement to the low-speed scenario [1]. In light of such limitations, the simplest and most intuitive solution is the adaptive material or structure that behaves in a multi-modal manner, which adjusts the system to absorb energy efficiently under various impact conditions.

To fulfill the multi-modal and self-adaptive requirement criteria, we draw inspiration from the traditional art of paper folding, known as the origami principle. This principle, renowned for its versatility and design flexibility for designing deployable or shape morphing structures [2–5], has proven effective in the exploration of origami-based mechanical metamaterials. To list a few exemplary properties, origami-inspired systems support load-bearing capability [4, 6–13], variable stiffness [14, 15], auxeticity [9, 16], and multi-stability [10, 17–21], most of which are highly tunable. Moreover, the origami principle facilitates mechanics-based structural design, where we can obtain desired mechanical properties simply by tailoring the geometry, e.g., crease patterns, of the constituting origami. Thus, origami-based designs can allow predictable geometrical morphing in response to external loading conditions. When used for impact mitigation purposes, a plethora of unconventional mechanical properties associated with various morphing stages can be leveraged to achieve multi-model deformation and adaptive energy absorption. This is in contrast to conventional energy absorption systems that deform in an unpredictable and inefficient manner, often relying on plastic deformation of the constituent material.

While origami-inspired materials offer promising pathways for sophisticated material design, most of the previous studies target either the static or quasi-static behavior of origami, except for very few predecessor works on waveguide [22–24] and vibration filtering [25–27]. However, these exceptions dealt with dynamics of origami limited to either small amplitude oscillation or a long-wave propagation in a chain of approximated continuum system. The study on simple energy-absorbing dynamics of the origami itself under the abrupt and large magnitude of load, commonly observed in the impact, is yet largely unexplored. Only recently, and limited to very few, the origami behavior in such an extreme dynamic scenario is considered, showing the potency of origami as the impact mitigation device [28, 29], which

leverages the crashworthiness of origami-inspired geometry, and not the folding behavior itself for energy absorption. Moreover, most of the commonly used origami architectures for dynamic studies do not take advantage of the rich morphology of origami in various tessellations, but are restricted to a mere assembly of simple origami units, such as Miura-ori [7], Yoshimura [6], Kresling origami [30], and Tachi-Miura polyhedron [31]), in a planar or stacked configuration. This, in turn, limits the origami-based structures to be considered for a wide range of structural members that necessitate curved geometries without being restricted to a polyhedral bulk profile.

In the present study, we investigate the dynamically—yet passively—tunable origami layer based on the Resch origami structure through numerical and experimental means. Resch-patterned origami, initially developed for versatile architectural surfaces [32, 33], achieves both flat and hemispherical surfaces during folding, enabling free-form morphing to program curvature [34–36]. While being studied on its complex high-degree-of-freedom shape morphing capability, the mechanical response of the Resch-patterned structure remains underinvestigated except for those that reported the usage of the Resch origami as the sandwich core structure under quasi-static loading [37–39]. Nonetheless, the load-carrying capability does not originate from the folding behavior of the Resch pattern; instead, it relies on plastic deformation to absorb energy. The mechanical response of the Resch origami under both static and dynamic load, dominated by its highly versatile free-form folding motion of the Resch origami itself, has remained obscure.

To address this indisputable knowledge gap, we first conduct an elastic folding simulation of the Resch origami to explore its highly versatile morphing behavior, which reveals a hemispherical morphing stage between flat states [32–34]. Such curved, yet developable, morphing behavior enables two distinct modes of the deformation: folding and unfolding modes, offering significantly different mechanical behavior between modes, such as monostable and bistable, and strain-softening and -hardening. Leveraging this distinctive response, we investigate the dynamic behavior of Resch origami under collision with a spherical impactor in the drop test. We report the dynamic bifurcation of the Resch origami triggered by the wide-ranging impact speeds. This is in contrast to some of the previously studied bifurcation of kinematic or static origami behavior [40–46]. Interestingly, the Resch origami reconfigures itself to follow a specific deformation path between multi-modes, dynamically bifurcating under impact and enabling the switching between folding and unfolding deforma-

tion modes across the critical impact speed. Such unique switching behavior can also be seen in the meter-scale prototype of the Resch origami tessellation that mimics an automotive bumper. Upon collision with the mannequin at different speeds, the Resch origami structure switches between folding and unfolding mode to minimize peak accelerations, suggesting the generality and universality of the energy absorption mechanism triggered by the dynamic bifurcation. We believe our findings shall bring new insight into the design methodology of smart impact mitigation devices featuring self-adaptivity to be employed in a wide spectrum of impact scenarios.

II. RESULTS

A. Physical set-up and modeling

In this study, we consider the Resch origami shown in Fig. 1a consisting of hexagonal panels (shaded with light grey) connected through triangular folding structures (shaded with dark grey), which we will refer to as startuck henceforth [34]. We primarily select the circular tiling pattern where the hexagonal facets are tessellated radially while maintaining the rotational symmetry. The folding directions are defined in Fig. 1a, where mountain and valley folds are denoted as black solid and dashed lines, respectively. As the crease pattern suggests, the geometry of the Resch origami is determined solely by the length parameter a , which is the side length of the hexagonal facets (see Fig. 1b).

The current configuration of the Resch origami shows a folding sequence that radially contracts while hexagonal facets rotate about their own centroid (see Supplementary Movie 1 for visual representation). Furthermore, the origami goes through a fully folded flat surface, a hemispherical surface, and then a fully deployed flat surface [32–34]. This folding process typically necessitates the non-rigid elastic behavior of the hexagonal and startuck facets. To capture such peculiar folding behavior and the corresponding mechanical responses, we employ the bar-hinge-mass model of origami [36, 47–50]. The model consists of three components: the axial bar element to describe non-rigid facet deformation, the torsional hinge element to model the crease folding, and the lumped mass assigned to each vertex of the facet to give an inertial property to the origami (see Methods section and Supplementary Note 1, and Supplementary Figure 1 for more detail of each element).

The resulting equation of motion of the i -th vertex (i.e., mass) of the origami reads,

$$m_i \ddot{\mathbf{u}}_i + \mathbf{F}_{i,\text{bar}} + \mathbf{F}_{i,\text{tor}} + \mathbf{F}_{i,\text{damp}} = \mathbf{F}_{\text{ext}}, \quad (1)$$

where m_i is the lumped mass, \mathbf{u}_i is the displacement vector, $\mathbf{F}_{i,\text{bar}}$ and $\mathbf{F}_{i,\text{tor}}$ are the internal forces due to axial spring and torsional spring deformation, respectively. Note that the axial bar stiffness is estimated based on the material properties [51], and the torsional spring stiffnesses are calibrated through a single hinge compression test (see Supplementary Note 2 and Supplementary Figure 4 for more detail). Any possible energy dissipation is governed by $\mathbf{F}_{i,\text{damp}}$ term, the details of which are laid out in Supplementary Note 1. The sum of the above left-hand-side terms balances with the external force \mathbf{F}_{ext} . This term can be zero for free unfolding simulation, gradually increasing over time for examining quasi-static response, or contact force with another object for the dynamic impact cases. (For more details on each term and derivation, see the Methods section and Supplementary Note 1 and Supplementary Figure 1-3.)

Figure 1c shows folding behavior obtained using the dynamic unfolding simulation via the aforementioned bar-hinge-mass model. Our simulation starts from the fully folded flat surface [sub-panel (i)]. The Resch origami then goes through the hemispherical profile [sub-panel (ii) and (iii)], which becomes a flat state when fully deployed [sub-panel (iv)]. Such behavior coincides well with the previously shown Resch origami behavior [32–34] (see also Supplementary Note 1, Supplementary Movie 1 for more information on the quasi-static unfolding behavior).

To quantitatively characterize the aforementioned folding sequence, we illustrate the relationship between two morphometric quantities h_c and γ in Fig. 1d. Here, the height h_c is defined as the out-of-plane distance between the centroid of the center hexagon and the outer hexagon along the out-of-plane direction. The height h_c varies as the Resch origami develops, which is described with the deployment ratio $\gamma = \frac{r - r^{(0)}}{r^{(1)} - r^{(0)}}$, where r is the radial distance from the origin to the centroid of the outer hexagons (see inset of Fig. 1d). Superscripts (0) and (1) denote the folded and deployed state, respectively. Therefore, $\gamma = 0$ ($\gamma = 1$) when fully folded (deployed). As γ varies from 0 to 1, h_c first increases monotonically until it reaches its peak ($h_{c,\text{max}} \approx 0.67a$) at the critical deployment ratio $\gamma_{\text{cr}} \approx 0.51$. After γ_{cr} , the height decreases and falls to zero when the Resch pattern is fully deployed, as shown in Fig. 1d.

Now, if we closely examine the folding behavior, we can see that it hints at two possible paths of deformation starting from the hemispherical configuration: folding and unfolding, with respect to the translational degree of freedom. In particular, consider loading the Resch pattern normal to the center hexagon (i.e., out-of-plane direction). Under such loading conditions, the Resch origami set at maximum $h_{c,\max}$ configuration (i.e., $h_c \approx 0.67a$, labeled (ii) in Fig. 1d) can either fold or unfold, both of which are a geometrically compatible path (labeled as ‘F-path’ and ‘U-path’, respectively). This dual-mode deformation, enabled by a predefined crease pattern, is in contrast to conventional planar structures that typically deform monotonously and unpredictably under loading. Such versatile dual-mode behavior will be investigated rigorously in quasi-static and dynamic loading conditions below.

B. Dual deformation mode and static response

We consider the scenario where the external load $\mathbf{F}_{\text{ext}} = \mathbf{P}_z$ is applied normal to the center hexagon of the Resch pattern. The initial state of the Resch pattern is set at the most convex posture (i.e., $h_{c,\max} = 0.67a$). We define the positive displacement u as the compression relative to maximum height (i.e., $u = h_{c,\max} - h_c$). The outer hexagons are fixed in the out-of-plane direction at their centroids to prevent the rigid body translation of the entire structure upon compression or tension. In Fig. 2a, we show a resulting bifurcation diagram as a function of u/a and γ . The color intensity of the bifurcation diagram represents the total potential energy stored in the origami, which is given by

$$U_{\text{total}} = \sum_i^{N_{\text{elem,bar}}} U_{i,\text{bar}} + \sum_i^{N_{\text{elem,tor}}} U_{i,\text{tor}}. \quad (2)$$

Here, $N_{\text{elem,bar}}$ and $N_{\text{elem,tor}}$ are the total number of axial bar and torsional spring elements, respectively, and $U_{i,\text{bar}}$ and $U_{i,\text{tor}}$ are their strain energy (see Supplementary Note 1.5 for more detail).

We observe that the potential energy well, denoted as a light grey solid line, splits into two under compression, the profile of which corresponds to the relationship between the height and deployment ratio shown in Fig. 1d. The bifurcation behavior in Fig. 2a can be categorized as a supercritical pitchfork bifurcation, where we have one stable equilibrium path before the bifurcation (in the current case, $u < 0$), which bifurcates into two stable equilibria with one unstable equilibrium path in between (dark grey dashed line). In

Fig. 2a, the upper and lower equilibrium paths are folding and unfolding equilibrium paths, respectively, corresponding to the ‘F-path’ and ‘U-path’ in the previous section.

Along each path, we conduct the uniaxial compression test by fabricating prototypes with a polyethylene terephthalate (PET) sheet. The PET sheets are cut by a laser cutter and then heat-processed to control the initial posture (See the Methods section, Supplementary Note 3, Supplementary Figures 5 and 6, and Supplementary Movie 2 for more details on the fabrication). Here, we use the Resch origami prototype initially configured to an 80% of the maximum height (i.e., $h_{c,0} = 0.8h_{c,\max}$) determined based on the quasi-static unfolding simulation result (shown in Fig. 1d). Note that at 80% height, we have two possible configurations: folding configuration ($\gamma < \gamma_{\text{cr}}$) and unfolding configuration ($\gamma > \gamma_{\text{cr}}$). Prescribing them along the F- or U-path ensures the deformation to follow the designated path, facilitating the evaluation of static response along each path.

The force-displacement curves as the compression test results are shown in Fig. 2b, where ‘F-path’ and ‘U-path’ are denoted as red and blue dashed lines, respectively. The first part of the deformation regime ($u/a < 0.8h_{c,\max} \approx 0.54$) is where the crease folding dominates the deformation; the grey-shaded region beyond the flat stage ($u/a > 0.54$) can be considered a highly non-rigid regime where the displacement exceeds the initial maximum height of the Resch origami and the deformation is dominated by the facet deformation. (For more details on the quasi-static uniaxial compression test setup and procedure, see the Methods section and Supplementary Note 4, Supplementary Figure 8, and Supplementary Movie 3.)

As can be seen, two paths show qualitatively distinct force-displacement landscapes. The folding path shows a monotonically increasing weakly strain-softening response followed by the sudden increase of the force after $u/a \approx 0.54$ due to the facet contact. Note that the force starts to rise a while after $u/a \approx 0.54$, which we believe is due to the facet bending before the densification dominates the mechanical behavior. Contrarily, the force in the unfolding path case first increases, decreases to negative force, and then increases again to $P_z > 0$ regime. This suggests that the folding path is monostable, and the unfolding path is bistable. We can confirm such multi-stability in Fig. 2c, where potential energy profiles are shown as a function of u/a . We can clearly see two minima (red triangle symbols) of the unfolding case, unlike the folding case with only one minimum at $u/a = 0$.

In Fig. 2d and e, we show the postures of the Resch origami during the compression along the folding and unfolding path, respectively. With the folding configuration, we can see that

the Resch origami deforms from a hemispherical convex shape into a flat-surface profile within the crease folding regime [Fig. 2d, sub-panel (i) into (ii)]. After this flat stage, the Resch pattern becomes a concave profile in the facet deformation regime where the structure “locks” due to the facet contact amongst those comprising the triangular startucks, as shown in Fig. 2d, sub-panel (iii). On the other hand, the unfolding configuration tends towards the flat deployed state first. Once the structure reaches flat state ($u = h_{c,0}$) [Fig. 2e, sub-panel (ii)], the origami halts deployment while the center hexagon continues to be pushed down further. Beyond this flat stage, the Resch origami becomes a concave shape (but intrinsically different from that of folding configuration), reaching and passing over the potential energy barrier between the first and the second stable points. Note that the flat state and the concave shape shown in Fig. 2e, sub-panel (ii) and (iii) corresponds to the local maximum and minimum potential energy shown in Fig. 2c. This is well described by the different postures between flat and concave postures. While the creases are almost all flattened for the flat state, the concave state contains some creases being slightly folded in the same direction as the initial state shown in sub-panel (i).

C. Folding and unfolding under impact

Given the bifurcation behavior and static response, we now investigate the response of the Resch origami subject to dynamic loads. Specifically, we conduct a drop test with the aforementioned folding and unfolding configurations (i.e., configured at $h_c = 0.8h_{c,\max}$) of the Resch origami subject to abrupt out-of-plane loads. As shown in Fig. 3a, the drop tower consists of three major components: (i) electromagnet-based release system, (ii) impactor, and (iii) Resch origami. The impactor is initially held with a pair of electromagnets, and released along the vertically fixed shaft when the electromagnets are switched off. The height at which the impactor is released is varied, such that the impactor collides with the center hexagon of the Resch pattern at a predefined impact speed (For more details on the drop test setup and procedure, see the Methods section and Supplementary Note 5, Supplementary Figure 9, and Supplementary Movie 4).

Figure 3b and 3c show the height of the impactor for the impact speed of 0.5 and 3.0 m/s, respectively. Here, dashed lines with shaded regions are experimental results, and solid lines are numerical simulation results. The numerical simulation is conducted using

the bar-hinge-mass model to capture the dynamic behavior of the origami that occurs in a relatively short period of time. Consequently, the right-hand-side of Eq. (1) for the impact test reads,

$$\mathbf{F}_{\text{ext}} = \mathbf{F}_{i,g} + \mathbf{F}_{i,\text{collision}}, \quad (3)$$

where the gravitational force $\mathbf{F}_{i,g}$ and external force due to collision $\mathbf{F}_{i,\text{collision}}$ are taken into account. Here, $\mathbf{F}_{\text{collision}}$ is determined based on the visco-elastic Hertzian model [52] between an elastic sphere and plane [53–56] (please refer to Supplementary Note 1.7 for more details).

At low impact speed, we can see that both folding and unfolding configurations show bouncing back motion, which triggers the oscillatory height profile in Fig. 3b. Particularly, the unfolding configuration does not deform beyond the crease folding regime indicated in the force-displacement curve in Fig. 2b, resulting in the motion around the first stable point. On the contrary, the higher impact speed case in Fig. 3c shows distinctive impactor motion between folding and unfolding configurations. The folding configuration shows an oscillatory trajectory due to a rebound similar to the low-speed case. In the unfolding configuration, however, the impactor subducts into the Resch origami and settles down without going through the major oscillatory response. Such behavior suggests the transition from the first stable state into the second stable state through large deformation (see Fig. 2c), unlike the relatively small amplitude of dynamics in the low-speed case where only the first stable state contributes to the dynamic response.

To unveil the mechanism of impact mitigation by the Resch origami, we visually examine the folding sequence of the Resch origami upon impact at $v_{\text{impact}} = 3.0$ m/s. Figure 3d and 3e show the snapshots of the Resch origami posture at the critical moments of the impact from the experiment, in the folding configuration and unfolding configuration, respectively. The corresponding moments from the numerical simulation are also shown in Fig. 3f and 3g (see Supplementary Note 7 for more details of the numerical methods and parameters). Each snapshot from the experiment corresponds to the time (i) $t = 0.306$, (ii) 0.326 , (iii) 0.455 s, as marked in Fig. 3c.

At the moment of impact [$t = 0.306$ s; Fig. 3d-g, sub-panel (i)], the Resch origami is still at its zero-energy state (therefore the impactor height is zero). In the folding configuration case, the impactor reaches its minimum height at $t = 0.326$ s [see Fig. 3d and 3f, sub-panel (ii)], and the Resch origami becomes subtly concave as opposed to its convex zero-energy

state posture. Such a concave profile is already out of the rigid-foldable regime of the Resch origami, which suggests the contribution of the panel deformation to the energy absorption process in addition to the crease folding (the height resides around $h/a = 1.26$, which is well beyond the rigid foldable limit). At $t = 0.455$ s, the Resch origami returns to its zero-energy state in the folding configuration, while the impactor reaches its maximum rebound height.

Contrarily, the impactor in the unfolding configuration does not show evident rebounding motions after the initial contact with the Resch pattern. Shortly after the impact, we observe the development of the Resch pattern into the flat unfolding state as shown in the sub-panel (ii) in Fig. 3e and 3g. Eventually, the prototype settles down to a state beyond the Resch origami at the second stable state [compare the deformation shapes between Fig. 2e, sub-panel (iii) and Fig. 3g, sub-panel (iii); see also Supplementary Movie 4 and 5 for the behavior of Resch pattern in the experiment and simulation, respectively]. This is also confirmed by the negative height profile of the impactor; the asymptotic height of the impactor is $h \approx -41.5$ mm (i.e., $h/a = -1.36$) in the unfolding Resch pattern's profile, which is past the position of the second stable point ($u/a \approx 0.73$) in the energy profile marked by a triangle in Fig. 2c. We believe that the deviation of asymptotic height from the second stable point is due to the mass of the impactor, which causes the equilibrium to shift. This can also be confirmed from the simulation result, where the asymptotic height resides around $h/a = 1.37$.

D. Dynamic bifurcation

In this section, we consider a dynamically bifurcating configuration of the Resch origami. Recall that, in Fig. 1d, we identified the maximum height of the Resch origami resides around $\gamma = 0.51$, which corresponds to the critical point in the bifurcation diagram in Fig. 2a. Based on this identified critical point, in the previous sections, we examined the behavior of the Resch origami along two different paths (i.e., folding and unfolding) by preconfiguring the Resch origami at 80% of the maximum height; two configurations are revealed to show very distinctive behavior in both static and dynamic regimes. Here, we investigate a dynamically bifurcating Resch origami by preconfiguring it at the bifurcating point (i.e., the maximum height configuration, $h_c = h_{c,\max}$).

Figure 4a-4c shows the height profiles of the impactor colliding with the Resch origami

at $v_{\text{impact}} = 2.0, 2.5,$ and 3.0 m/s, respectively. At a lower speed of the collision (see Fig. 4a), the impactor rebounds back to $h > 0$ after the collision, which is a signature of the folding type of the response. However, when the impact speed increases, for instance, to $v_{\text{impact}} = 2.5$ m/s, the Resch origami shows a versatile response to the impactor collision. Interestingly, the Resch origami shows both folding and unfolding motion in response to the collision at 2.5 m/s, as distinctive impactor trajectories suggest in Fig. 4b. When folded, the impactor shows the aforementioned signature of the folding response, the oscillatory rebound trajectory, denoted by the blue dashed line in Fig. 4b. Indicated by the purple dashed line is the case where the Resch origami unfolds, but does not pass through the energy barrier before the second stable state. Similar to the $v_{\text{impact}} = 0.5$ m/s case with unfolding configuration shown in Fig. 3b, the impactor trajectory shows an oscillatory profile with lower rebound height than the folding case. Lastly, the snap-through trajectory shows a rather sudden stop of the impactor without evident oscillatory motions, as denoted by the red dashed line in Fig. 4b. For such cases, the Resch origami resides in the second stable state, unlike the previous two scenarios. Thus, we see three major responses at the impact speed of interest. Now, if we further increase the impact speed up to 3.0 m/s, we only see the snap-through response as the dominant deformation mode, as shown in Fig. 4c. The impactor trajectory clearly shows the hallmark of the snap-through, where the impactor does not bounce back. As such, the Resch origami configured at the bifurcation point switches its deformation mode subject to the impact, depending on its speed.

In Fig. 4d, we show the number of occurrences of folding and unfolding modes out of 15 trials for each impact speed. At low impact speed ($v_{\text{impact}} = 0.5$ to 1.5 m/s), we only see folding mode response. For the trials in $v_{\text{impact}} = 2.0$ m/s case, we can still see the folding mode as the dominant response mode, except for the one trial where the Resch origami unfolds. At the critical impact speed of 2.5 m/s, we can see five folding and ten unfolding mode response trials, respectively. Among the ten unfolding situations, eight cases undergo the snap-through mechanism. This observation suggests the switching into the dominance of the snap-through mode, resulting in fourteen out of fifteen cases (93.3%) at $v_{\text{impact}} = 3.0$ m/s.

To investigate this self-adaptive mechanism of bifurcation depending on the impact speed, we revisit the deformation sequence of the Resch origami under impact in Fig. 4e, where the folding and unfolding trials of $v_{\text{impact}} = 2.5$ m/s case are shown. As briefly mentioned in the

previous section, the first phase of the deformation sequence is the contact phase [Fig. 4e, sub-panel (i)]. The impactor then continues to fall while pushing the center hexagon of the Resch origami as Fig. 4e, sub-panel (ii) shows, where the top and bottom rows show folding and unfolding trials, respectively. We refer to this second step as a subduction phase. Note that the outer hexagon translates neither inward nor outward during the subduction phase. We can confirm this by examining the red and blue vertical arrows indicating the centroid of the outer hexagons. As shown in Fig. 4e, sub-panel (ii), the arrows from the top and bottom rows overlap, implying that the outer hexagons are at the same position for folding and unfolding cases. The third step is the activation step for the outer hexagons, which either contract or expand, radially translating into or away from the center hexagon. If we track the centroid arrows, we can see that the locations of the center hexagons do not coincide between folding and unfolding cases. This deformation sequence suggests that the outer hexagons do not immediately respond to the impact, but activate after substantial deformation of the center hexagon. This is plausible because the central hexagon is surrounded by the outer hexagons through folded—thus highly compliant—startucks, incurring relative rotation and translation with respect to each other.

To explore the effect of this delayed activation of outer hexagons upon impact, we show the direction of the radial force exerted on the outer hexagons as a function of the center hexagon’s out-of-plane displacement in Fig. 4f. The radial force is obtained by conducting a quasi-static numerical simulation of the Resch origami, with outer hexagons being fixed in all translational directions at their centroid (see Methods section and Supplementary Note 7 for the detail). By imposing such constrained centroid conditions, we simulate the subduction phase where the outer hexagons are at rest. In Fig. 4f, we can see that the direction of radial force changes at different levels of subduction. Specifically, the radial force is negative below subduction displacement $u/a \approx 0.67$, indicating that the outer hexagons are experiencing the inward radial force, which is folding direction. After $u/a \approx 0.67$, the radial force becomes positive, where the outward force is exerted on the outer hexagons. This suggests that Resch origami follows different deformation modes depending on the subduction displacement, which is affected by the magnitude of the impulsive force (i.e., velocity) upon collision. We note in passing that this threshold subduction displacement roughly corresponds to the maximum height of the Resch origami, suggesting the switching occurs near the flat state of the Resch origami. Furthermore, recall that in the bifurcation diagram in Fig. 2a, the

unstable equilibrium path runs between the ‘F-path’ and ‘U-path.’ The unstable path first shows a slight deviation from γ_{cr} (see violet dashed line in Fig. 2a) towards the U-path at $0.0 < u/a < 0.59$. Contrarily, for $u/a > 0.59$, the unstable path is significantly indented towards F-path. This suggests that Resch origami under the subduction phase tends to fall into F-path (U-path) potential energy well for small (large) subduction displacement.

To exemplify the folding and unfolding case, we extract subduction displacement of $v_{\text{impact}} = 2.0$ and 3.0 cases from empirical data. The grey vertical dashed lines with shaded regions in Fig. 4f labeled (i) and (ii) are the average of the folding and unfolding trials from 2.0 and 3.0 m/s impact speed scenarios, respectively [corresponding to schematic diagrams in sub-panels (i) and (ii)]. We can clearly see that $v_{\text{impact}} = 2.0$ m/s case experiences an inward radial force with $u/a = 0.57 \pm 0.051$ subduction, and outward radial force for 3.0 m/s case with $u/a = 0.98 \pm 0.066$ subduction. This well suggests the contribution of subduction displacement and the associated direction of radial forces to the bifurcation of Resch origami deformation mode as a function of impact speed.

Such dynamic bifurcation offers unique behavior compared to the conventional material, as shown in Fig. 4g. Here, we estimate the coefficient of restitution (COR) based on the impact velocity and restitution velocity of the impactor as follows:

$$\text{COR} = \left| \frac{v_r}{v_{\text{impact}}} \right|. \quad (4)$$

where v_{impact} and v_r represent the velocity at the moment of impact and bounce back, respectively. The COR is collected for the bifurcation configuration of Resch origami. We also measure COR for extruded polystyrene foam (EPS; also known as styrofoam), one of the common energy absorption materials, for reference. Here, the EPS sample is fabricated by slicing the EPS into specific thickness (18 mm), such that it has the same mass and projected area as the fully unfolded Resch origami (see Methods section and Supplementary Note 3 for the detail of the EPS sample fabrication). While the EPS sample in grey cross symbols shows the almost plateau COR profile throughout the given velocity range, the Resch origami COR generally decreases as the impact speed increases for the bifurcating configuration in the folding mode (blue square symbol), hinting at better energy absorption in the higher impact speed scenarios. Moreover, switching from folding mode to unfolding mode around $v_{\text{impact}} = 2.5$ m/s (from blue data set to purple data set) further reduces the COR for improved energy absorption. Remarkably, when the snap-through mechanism

is triggered (red data set), the COR values significantly decrease, approaching near zero restitution (for other impact mitigation performance indices, see Supplementary Note 8 and Supplementary Figure 10). This manifests the efficacy of the multi-modal Resch origami structure for a broad range of impact conditions.

E. Meter-scale Resch origami tessellation for impact mitigation

We further evaluate the versatility of the Resch-patterned origami by fabricating a meter-scale Resch origami tessellation prototype. Figure 5a shows a pendulum-based experimental setup with Resch origami tessellation, mimicking a pedestrian impact with an automotive bumper. The system consists of two pendulums: one with Resch tessellation (rectangular tessellation with 11×6 hexagons as shown in Fig. 5b with a scale bar) and the other with a 3D-printed mannequin leg (for the details of the test setup, Resch origami tessellation and mannequin leg fabrication, please refer to Methods section, Supplementary Note 6, Supplementary Figure 7 and 10, and Supplementary Movie 2). Given that the behavior of our interest is adaptive bifurcation depending on impact speed, we consider low- and high-speed cases. The impact speed is controlled by the initial mannequin angle $\psi_{\text{mannequin}}^{(0)}$ (see Fig. 5a for the definition of the pendulum angle), which is set to 40.9° and 57.8° for low and high impact speed cases, respectively. The other pendulum with the Resch origami tessellation is initially at rest in vertical position (i.e., $\psi_{\text{Resch}}^{(0)} = 0^\circ$). Similar to the orbital Resch origami, we consider three different configurations: folding, unfolding, and bifurcating configuration by adjusting the width of the pendulum where the Resch tessellation is mounted. As a general rule, narrower widths tend to induce folding behavior, while wider widths are inclined to unfolding behavior; the intermediate case corresponds to the bifurcating configuration. Specifically, they are set to a deployment ratio based on the width as $\gamma_W = \frac{1}{N_{\text{col}}} \frac{W - W^{(0)}}{W^{(1)} - W^{(0)}} \approx 0.35, 0.50,$ and 0.55 , for folding, bifurcating, and unfolding configurations, respectively. Here, $N_{\text{col}} = 11$ is the number of columns of the tessellation, W is the width between the centroid of hexagons at the leftmost and the rightmost columns, and the superscripts (0) and (1) denoted folded and deployed state. We note in passing that the bifurcating configurations reside at similar values in both orbital and rectangular tessellation, as indicated by $\gamma \approx 0.51$ and $\gamma_W \approx 0.50$.

We confirm that, for a narrow configuration, the Resch tessellation only exhibits the

folding response. Contrarily, the widest configuration only shows an unfolding response (see Supplementary Movie 6 and 7 for the response of folding and unfolding configurations). Notably, the bifurcating configuration shows switching from folding to unfolding mode as the impact speed increases. Figure 5c details such deformation sequence of the bifurcating Resch tessellation at low- and high-speed impact scenarios (top and bottom rows, respectively). At the low impact speed, we can see that the center section of the tessellation contracts upon the collision with the mannequin leg, as shown in Fig. 5c, sub-panel (ii). After the kinetic energy of the mannequin is converted to the elastic strain energy of the Resch origami, the Resch origami restores to its original convex profile (i.e., zero-energy state), causing the mannequin to bounce back. In contrast, the high impact speed case does not show the contraction of the center area of the Resch tessellation but instead expands due to the unfolding reaction of the Resch origami [Fig. 5c, sub-panel (iv)]. Comparing Fig. 5c, sub-panel (ii) and (iv), we can clearly see the different morphological appearances; particularly, if we observe the distance from the top and bottom sides near the center of the Resch tessellation, we witness the expansion of the tessellation in the high-speed case [sub-panel (iv)], whereas the subtle contraction in the low-speed case [sub-panel (ii)]. Moreover, unlike the restoration of Resch tessellation in a low-speed-impact folding case, the center region of the Resch origami tessellation transitions into a second stable state, as shown in Fig. 5c, sub-panel (v) (for more details on the bifurcating Resch origami deformation in the pendulum system, see Supplementary Movie 8).

To quantitatively examine the Resch origami behavior and performance upon impact, we show the pendulum acceleration relative to the Resch origami, for all three configurations under low- and high-speed impact cases in Figure. 5d, sub-panel (i) and (ii), respectively. At low impact speed [Fig. 5d, sub-panel (i)], we see that the unfolding configuration experiences the largest magnitude of acceleration, followed by the bifurcating and, lastly, the folding configuration. Thus, the folding configuration handles the low-speed impact most efficiently. At high impact speed, conversely, the folding configuration undergoes the acceleration of the largest magnitude, and the unfolding configuration shows the least magnitude. This implies that the unfolding mode copes with the high speed impact better than the folding mode.

Such change in the aligning order of the acceleration can also be observed by extracting the peak acceleration. Figure 5e shows the peak acceleration magnitude $|a_{\text{peak}}|$ for the three configurations of the Resch alongside the EPS sample for low and high impact speed cases.

At a glance, we notice the lower peak acceleration (almost half) compared to the EPS sample. As mentioned earlier, we observe the intersection of the acceleration lines between the folding and unfolding configurations (denoted by blue and red data sets), demonstrating the efficacy of the folding (unfolding) mode for low (high) speed impact. More notably, the acceleration line for the bifurcating sample resides between these two lines. As illustrated by the inset images, the bifurcating sample selects the folding configuration for the low-speed impact while taking the unfolding mode for the high-speed impact. This validates that the Resch-patterned origami adaptively selects and morphs into the favorable deformation mode to minimize the peak acceleration upon impact. Thus, the pendulum test on the meter-scale Resch origami well suggests the potential applicability of the load-dependent bifurcation mechanism of the Resch pattern, not only to a small orbital configuration but also to a larger rectangular tiling that mimics a bumper system.

III. DISCUSSION

We have demonstrated the dynamically reconfigurable response of the Resch origami pattern, achieved through in-situ adaptation depending on external stimuli. We first focused on a simple orbital Resch origami structure through experimental and numerical means. We used a modified bar-hinge-mass model to capture its folding/unfolding motion, static response, and dynamic response to out-of-plane loads. The folding behavior and the bifurcation diagram have identified two modes of deformation (folding and unfolding), which in turn show highly distinctive force and potential energy landscapes in the uni-axial compression test; folding mode hosts a monostable response with strain softening, and unfolding mode offers a bistable response with snap-through. We have examined such distinctive mechanisms of deformation by conducting the drop test with different impact speeds and initial configurations of the Resch origami. While the folding configuration restores the original posture and pushes the impactor back into the air due to its monostability, the unfolding configuration has demonstrated the near-zero coefficient of restitution by going through the snap-through of the Resch origami in high-speed impact cases. Furthermore, unlike the mono-modal folding and unfolding configuration, the bifurcating configuration has exhibited a noteworthy dual-modality, which enables velocity-dependent self-reconfiguration. At low impact speed, the bifurcating configuration has shown a folding mode of deformation.

Contrarily, we have observed that the Resch origami unfolds and then snaps through at a higher speed of impact. This in-situ switching of deformation mode is induced by a peculiar deformation sequence associated with the switching direction of radial force from contraction to expansion.

In a simulated test of pedestrian impact, we confirm that the tessellation of the Resch origami structure also exhibited such bifurcation-driven behavior, transitioning from folding for low impact speed to unfolding for high speed. Additionally, the tessellated Resch origami structure hinted at the self-adaptive feature of the Resch-inspired structure subjected to the external load, where the switching from folding to unfolding mode automatically adjusts the structure to experience reduced peak acceleration. We believe that such adaptive nature of the Resch origami upon the dynamic load shall proffer an insight into opening a new avenue to designing self-reconfiguring adaptive impact mitigation devices.

METHODS

Fabrication

Resch origami prototypes (both orbital and rectangular) were laser-cut from 0.254 mm thick polyethylene terephthalate (PET) and hand-folded based on the crease pattern shown in Fig. 1a. The initial posture of the orbital Resch origami is controlled by heat treatment in a convection oven at 80°C for three hours, using 3D-printed custom support structures designed from simulated Resch origami posture. For the pendulum test, approximately 800 × 500 mm PET sheet was laser-cut and manually folded, resulting in the projected dimension of approximately 550 × 350 mm length and width.

The EPS samples are fabricated manually using hot wire, first by adjusting the thickness of the EPS block to approximately 18 mm and then cut into a fully deployed Resch origami profile for orbital Resch drop test. For the pendulum test, the EPS hexahedral block is fabricated in a similar manner, resulting in the dimension of 600 × 300 × 50 mm in length, width, and thickness. (For more details of each component and design, see Supplementary Note 3 and Supplementary Figure 5, 6, and 7.)

A. Experimental methods

To evaluate the orbital Resch origami’s response under compression and impact, we conducted quasi-static compression tests and drop tests. In both setups, the central hexagon is fixed at its centroid, allowing surrounding hexagons to move radially during deformation. During compression tests, a linear stage attached to the centroid of the center hexagon applies controlled displacement along the out-of-plane direction, while a load cell and laser sensor measure the resulting force and displacement. For the drop test, high-speed cameras capture the trajectory of the hemispherical impactor, dropped along the vertical shaft, which also fixes the center hexagon at its centroid. The trajectory of the impactor is then extracted by tracking the markers attached to the impactor through the digital image correlation (DIC). A pendulum-based impact test employs a two-pendulum system to simulate a pedestrian impact. Similar to the drop test, the motion of the pendulums was tracked using high-speed cameras and analyzed through DIC marker tracking. (For detailed descriptions of specific components, assembly methods, and additional visualizations, please refer to Supplementary Notes 3, 4, and 6.)

Numerical methods

We employ an origami model consisting of an axial bar, torsional hinge, and lumped mass in this study (for more details on formulation, see Supplementary Note 1). Unlike previous bar-hinge-mass models focusing kinematic behavior of origami [36, 57], the current study aims to simulate dynamic impact events and the corresponding deformations occurring in a short period of time (i.e., millisecond order). To this end, we extended the bar-hinge-mass model by incorporating additional factors such as gravitational force and visco-elastic collision force. The formulated model is then implemented by developing an in-house computer simulation code with Python and Fortran. Due to the stiff nature of Eq. (1), we employ the adaptive Runge-Kutta-Prince-Dormand method of 8th order accuracy with 3rd and 5th order error estimator [58], for the sake of better convergence. The maximum time step size of $\Delta t = 10^{-5}$ s and relative and absolute error tolerance $\epsilon = 10^{-12}$ are used. All numerical values are treated as double-precision float point numbers.

ACKNOWLEDGMENTS

We acknowledge financial support from the Toyota Research Institute North America. K.Y., Y.M., and J.Y. also thank the financial support from the U.S. National Science Foundation under Grant No. CMMI-1933729 and -2201612. Y.M., S.K., M.C., J.K., M.K., and J.Y. acknowledge the support from National Research Foundation grants funded by the Korean government [2022H1D3A2A03096579 and 2023R1A2C2003705]. We also thank Mr. Yasuhito Miyazawa for his insightful comments on the experimental setup design.

AUTHOR CONTRIBUTIONS

Y.M. and J.Y. conceived the project; Y.M., Y.S., S.S., U.G., and J.Y. conceptualized the project; Y.M. and C.-Y.C. explored the theoretical framework; Y.M., Q.L., R.T.A., K.Y., J.K., M.C., S.K., and M.K. conducted the experiment; Y.M. analyzed experimental results, developed the software code, carried out numerical simulation, and prepared the original draft of the manuscript; All authors extensively contributed to revising and finalizing the manuscript; J.Y. supervised the project.

COMPETING INTERESTS

The authors declare no competing interests.

DATA AVAILABILITY

Data supporting the findings of this study are available in the Zenodo repository under the accession code <https://doi.org/10.5281/zenodo.10910268>.

COMPUTER CODE AVAILABILITY

Computer codes developed to generate the results of this study are available in the Zenodo repository under the accession code <https://doi.org/10.5281/zenodo.10910268>.

REFERENCES

- [1] M. M. Davoodi, S. M. Sapuan, A. Aidy, N. A. Abu Osman, A. A. Oshkour, and W. A. Wan Abas, Development process of new bumper beam for passenger car: A review, [Materials and Design](#) **40**, 304 (2012).
- [2] R. J. Lang, S. Magleby, and L. Howell, Single degree-of-freedom rigidly foldable cut origami flashers, [Journal of Mechanisms and Robotics](#) **8**, 10.1115/1.4032102 (2016).
- [3] W. Kim, J. Byun, J.-K. Kim, W.-Y. Choi, K. Jakobsen, J. Jakobsen, D.-Y. Lee, and K.-J. Cho, Bioinspired dual-morphing stretchable origami, [Science Robotics](#) **4**, 3493 (2019).
- [4] D. Y. Lee, J. K. Kim, C. Y. Sohn, J. M. Heo, and K. J. Cho, High-load capacity origami transformable wheel, [Science Robotics](#) **6**, 201 (2021).
- [5] Z. Li, Q. Yang, R. Fang, W. Chen, and H. Hao, Origami metamaterial with two-stage programmable compressive strength under quasi-static loading, [International Journal of Mechanical Sciences](#) **189**, 105987 (2021).
- [6] Yoshimura Yoshimaru, *National Advisory Committee for Aeronautics Technical memorandum*, Tech. Rep. (National Advisory Committee for Aeronautics, Washington, 1955).
- [7] M. Schenk and S. D. Guest, Geometry of Miura-folded metamaterials, [Proceedings of the National Academy of Sciences](#) **110**, 3276 (2013).
- [8] K. Saito, S. Pellegrino, and T. Nojima, Manufacture of Arbitrary Cross-Section Composite Honeycomb Cores Based on Origami Techniques, [Journal of Mechanical Design](#) **136**, 10.1115/1.4026824 (2014).
- [9] H. Yasuda and J. Yang, Reentrant Origami-Based Metamaterials with Negative Poisson's Ratio and Bistability, [Physical Review Letters](#) **114**, 185502 (2015).
- [10] Y. Yang, M. A. Dias, and D. P. Holmes, Multistable kirigami for tunable architected materials, [Physical Review Materials](#) **2**, 110601 (2018).
- [11] J. Zhang, D. Karagiozova, Z. You, Y. Chen, and G. Lu, Quasi-static large deformation compressive behaviour of origami-based metamaterials, [International Journal of Mechanical Sciences](#) **153-154**, 194 (2019).
- [12] Z. Li, Q. Yang, R. Fang, W. Chen, and H. Hao, Origami metamaterial with two-stage programmable compressive strength under quasi-static loading, [International Journal of Mechanical Sciences](#) **189**, 10.1016/j.ijmecsci.2020.105987 (2021).

- [13] A. Jamalimehr, M. Mirzajanzadeh, A. Akbarzadeh, and D. Pasini, Rigidly flat-foldable class of lockable origami-inspired metamaterials with topological stiff states, [Nature Communications](#) **13**, 1816 (2022).
- [14] T. Mukhopadhyay, J. Ma, H. Feng, D. Hou, J. M. Gattas, Y. Chen, and Z. You, Programmable stiffness and shape modulation in origami materials: Emergence of a distant actuation feature, [Applied Materials Today](#) **19**, 100537 (2020).
- [15] Y. Miyazawa, H. Yasuda, H. Kim, J. H. Lynch, K. Tsujikawa, T. Kunimine, J. R. Raney, and J. Yang, Heterogeneous origami-architected materials with variable stiffness, [Communications Materials](#) **2**, 110 (2021).
- [16] Y. Zheng, I. Niloy, P. Celli, I. Tobasco, and P. Plucinsky, Continuum Field Theory for the Deformations of Planar Kirigami, [Physical Review Letters](#) **128**, 208003 (2022).
- [17] J. L. Silverberg, A. A. Evans, L. McLeod, R. C. Hayward, T. Hull, C. D. Santangelo, and I. Cohen, Using origami design principles to fold reprogrammable mechanical metamaterials, [Science](#) **345**, 647 (2014).
- [18] L. S. Novelino, Q. Ze, S. Wu, G. H. Paulino, and R. Zhao, Untethered control of functional origami microrobots with distributed actuation, [Proceedings of the National Academy of Sciences](#) **117**, 24096 (2020).
- [19] D. Melancon, B. Gorissen, C. J. García-Mora, C. Hoberman, and K. Bertoldi, Multistable inflatable origami structures at the metre scale, [Nature](#) **592**, 545 (2021).
- [20] J. E. Suh, Y. Miyazawa, J. Yang, and J. H. Han, Self-Reconfiguring and Stiffening Origami Tube, [Advanced Engineering Materials](#) **24**, 2101202 (2022).
- [21] N. Hu, B. Li, R. Bai, K. Xie, and G. Chen, A Torsion-Bending Antagonistic Bistable Actuator Enables Untethered Crawling and Swimming of Miniature Robots, [Research](#) **6**, 10.34133/research.0116 (2023).
- [22] H. Yasuda, Y. Miyazawa, E. G. Charalampidis, C. Chong, P. G. Kevrekidis, and J. Yang, Origami-based impact mitigation via rarefaction solitary wave creation, [Science Advances](#) **5**, eaau2835 (2019), [arXiv:1805.05909](#).
- [23] D. F. Wang, Y. Q. Wang, Z. H. Qian, T. Tachi, and K. C. Chuang, A graded Miura-ori phononic crystals lens, [Physics Letters, Section A: General, Atomic and Solid State Physics](#) **418**, 10.1016/J.PHYSLETA.2021.127701 (2021).

- [24] Y. Miyazawa, C.-W. Chen, R. Chaunsali, T. S. Gormley, G. Yin, G. Theocharis, and J. Yang, Topological state transfer in Kresling origami, [Communications Materials](#) **3**, 62 (2022).
- [25] M. Zhang, J. Yang, and R. Zhu, Origami-Based Bistable Metastructures for Low-Frequency Vibration Control, [Journal of Applied Mechanics](#) **88**, 10.1115/1.4049953 (2021).
- [26] J. C. Ji, Q. Luo, and K. Ye, Vibration control based metamaterials and origami structures: A state-of-the-art review, [Mechanical Systems and Signal Processing](#) **161**, 107945 (2021).
- [27] X. Yu and L. Wang, Nonlinear dynamics of coupled waves in Kresling origami metamaterials, [Journal of Sound and Vibration](#) **577**, 118263 (2024).
- [28] S. Tomita, K. Shimanuki, S. Oyama, H. Nishigaki, T. Nakagawa, M. Tsutsui, Y. Emura, M. Chino, H. Tanaka, Y. Itou, and K. Umemoto, Transition of deformation modes from bending to auxetic compression in origami-based metamaterials for head protection from impact, [Scientific Reports](#) **13**, 12221 (2023).
- [29] Q. Yang, Z. Li, H. Hao, and W. Chen, Compressive mechanical properties and dynamic behaviour of origami-inspired tri-directional auxetic metastructure, [Engineering Structures](#) **281**, 115751 (2023).
- [30] B. Kresling, Origami-structures in nature: lessons in designing “smart” materials, [MRS Proceedings](#) **1420**, mrsf11 (2012).
- [31] K. Miura and T. Tachi, Synthesis of rigid-foldable cylindrical polyhedra, [J. ISIS-Symmetry, Spec. Issues Festival-Congress Gmuend, Austria](#) , 204 (2016).
- [32] R. D. Resch and H. Christiansen, The design and analysis of kinematic folded-plate systems, in [Proceedings of the Symposium for folded plates and prismatic structures, International association for shell structures](#) (1970) pp. 1–36.
- [33] R. D. Resch, The topological design of sculptural and architectural systems, in [Proceedings of the June 4-8, 1973, national computer conference and exposition on - AFIPS '73](#) (ACM Press, New York, New York, USA, 1973) p. 643.
- [34] T. Tachi, Designing freeform origami tessellations by generalizing resch’s patterns, [Journal of Mechanical Design, Transactions of the ASME](#) **135**, 10.1115/1.4025389 (2013).
- [35] F. Yang, M. Zhang, J. Ma, Z. You, Y. Yu, Y. Chen, and G. H. Paulino, Design of Single Degree-of-Freedom Triangular Resch Patterns with Thick-panel Origami, [Mechanism and Machine Theory](#) **169**, 104650 (2022).

- [36] Y. Yu, Y. Chen, and G. Paulino, Programming curvatures by unfolding of the triangular Resch pattern, [International Journal of Mechanical Sciences](#) **238**, 107861 (2023).
- [37] M. A. E. Kshad, C. Popinigis, and H. E. Naguib, 3D printing of Ron-Resch-like origami cores for compression and impact load damping, [Smart Materials and Structures](#) **28**, 015027 (2019).
- [38] A. Deng, B. Ji, X. Zhou, and Z. You, Geometric design and mechanical properties of foldcores based on the generalized Resch patterns, [Thin-Walled Structures](#) **148**, 106516 (2020).
- [39] Z. Chen, T. Wu, G. Nian, Y. Shan, X. Liang, H. Jiang, and S. Qu, Ron resch origami pattern inspired energy absorption structures, [Journal of Applied Mechanics, Transactions ASME](#) **86**, 11005 (2019).
- [40] I. Ario and M. Nakazawa, Non-linear dynamic behaviour of multi-folding microstructure systems based on origami skill, [International Journal of Non-Linear Mechanics](#) **45**, 337 (2010).
- [41] S. Farah, D. G. Anderson, and R. Langer, Physical and mechanical properties of PLA, and their functions in widespread applications — A comprehensive review, [Advanced Drug Delivery Reviews](#) **107**, 367 (2016).
- [42] A. Gillman, K. Fuchi, and P. Buskohl, Truss-based nonlinear mechanical analysis for origami structures exhibiting bifurcation and limit point instabilities, [International Journal of Solids and Structures](#) **147**, 80 (2018).
- [43] S. Sadeghi and S. Li, Dynamic folding of origami by exploiting asymmetric bi-stability, [Extreme Mechanics Letters](#) **40**, 100958 (2020).
- [44] L. Zhang, F. Pan, Y. Ma, K. Yang, S. Guo, and Y. Chen, Bistable reconfigurable origami metamaterials with high load-bearing and low state-switching forces, [Extreme Mechanics Letters](#) **63**, 102064 (2023).
- [45] Y. Wang and K. Liu, Shape optimization of non-rigid origami leading to emerging bistability, [Mechanics Research Communications](#) **132**, 104165 (2023).
- [46] Q. Zhang, J. Cai, X. Deng, Z. Qian, and J. Feng, Kinematic Solutions and Bifurcation Analysis of Single Vertex Origami Pattern, [Mechanics Research Communications](#) **135**, 104238 (2024).
- [47] K. Liu and G. H. Paulino, Nonlinear mechanics of non-rigid origami: an efficient computational approach, [Proceedings of the Royal Society A: Mathematical, Physical and Engineering Sciences](#) **473**, 20170348 (2017).
- [48] S. Dong and Y. Yu, Numerical and experimental studies on capturing behaviors of the inflatable manipulator inspired by fluidic origami structures, [Engineering Structures](#) **245**, 112840

(2021).

- [49] S. Dong, X. Zhao, and Y. Yu, Dynamic unfolding process of origami tessellations, *International Journal of Solids and Structures* **226-227**, [10.1016/j.ijsolstr.2021.111075](https://doi.org/10.1016/j.ijsolstr.2021.111075) (2021).
- [50] Y. Xia, N. Kidambi, E. Filipov, and K. W. Wang, Deployment Dynamics of Miura Origami Sheets, *Journal of Computational and Nonlinear Dynamics* **17**, [10.1115/1.4054109](https://doi.org/10.1115/1.4054109) (2022).
- [51] K. Liu and G. H. Paulino, Highly efficient nonlinear structural analysis of origami assemblages using the MERLIN2 software, *Origami* **7**, 1167 (2018).
- [52] Y. Gonthier, J. McPhee, C. Lange, and J.-C. Piedbœuf, A Regularized Contact Model with Asymmetric Damping and Dwell-Time Dependent Friction, *Multibody System Dynamics* **11**, [209](https://doi.org/10.1007/s00034-004-0209-0) (2004).
- [53] W. Goldsmith, *Impact: The Theory and Physical Behavior of Colliding Solids* (Edward Arnold, London, 1960).
- [54] M. Machado, P. Moreira, P. Flores, and H. M. Lankarani, Compliant contact force models in multibody dynamics: Evolution of the Hertz contact theory, *Mechanism and Machine Theory* **53**, 99 (2012).
- [55] H. Hertz, Über die Berührung fester elastischer Körper, *Journal für die reine und angewandte Mathematik* **92**, 156 (1881).
- [56] H. R. Hertz, Über die Berührung fester elastischer Körper und über die Härte, *Verhandlungen des Vereins zur Beförderung des Gewerbefleißes, Berlin : Verein zur Beförderung des Gewerbefleißes* , 449 (1882).
- [57] Y. Zhu and E. T. Filipov, An efficient numerical approach for simulating contact in origami assemblages, *Proceedings of the Royal Society A: Mathematical, Physical and Engineering Sciences* **475**, 20190366 (2019).
- [58] E. Hairer, G. Wanner, and S. P. Nørsett, *Solving Ordinary Differential Equations I*, Springer Series in Computational Mathematics, Vol. 8 (Springer Berlin Heidelberg, Berlin, Heidelberg, 1993).

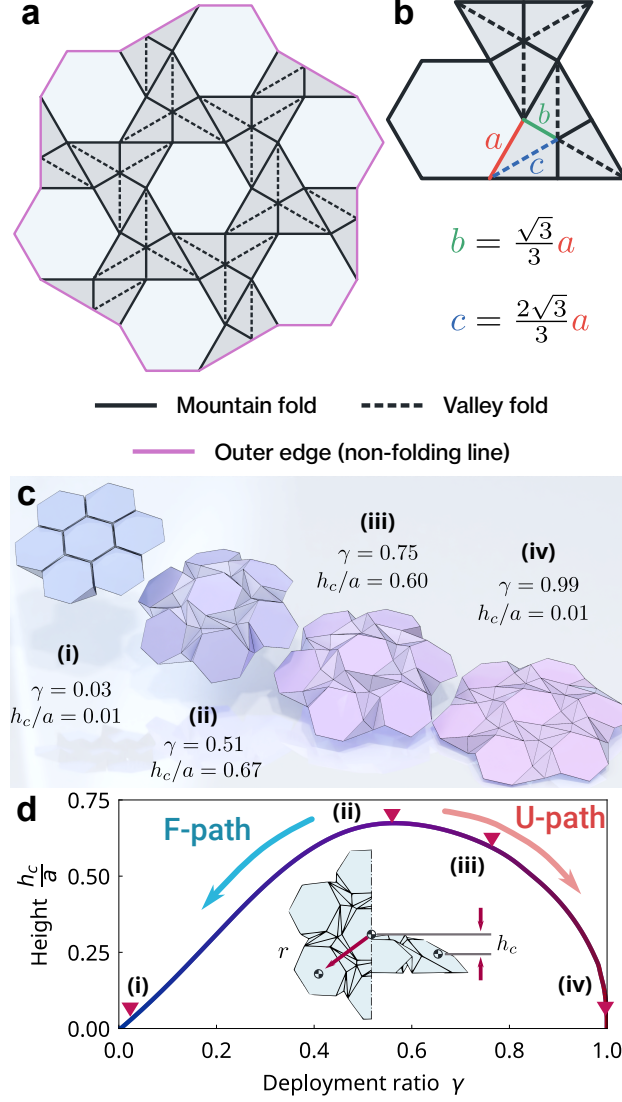


FIG. 1. The schematic illustrations of the hexagon-triangle Resch origami and its folding motion. (a) Folding pattern of the single-orbit hexagon-triangle Resch pattern. (b) Definition of geometrical parameters. The geometry of the hexagon-triangle Resch pattern is determined solely by the side length of the hexagon a . The lengths of minor and major crease b and c within the startuck are determined as $b = \frac{\sqrt{3}}{3}a$ and $c = \frac{2\sqrt{3}}{3}a$, respectively. (c) Folding motion of Resch origami. (d) Variation of normalized height h_c/a as a function of deployment ratio γ . Sub-labels are at (i) $h_c/a = 0.01$, (ii) 0.67, (iii) 0.6, and (iv) 0.01, which correspond to $\gamma = 0.03, 0.51, 0.75,$ and $0.99,$ respectively.

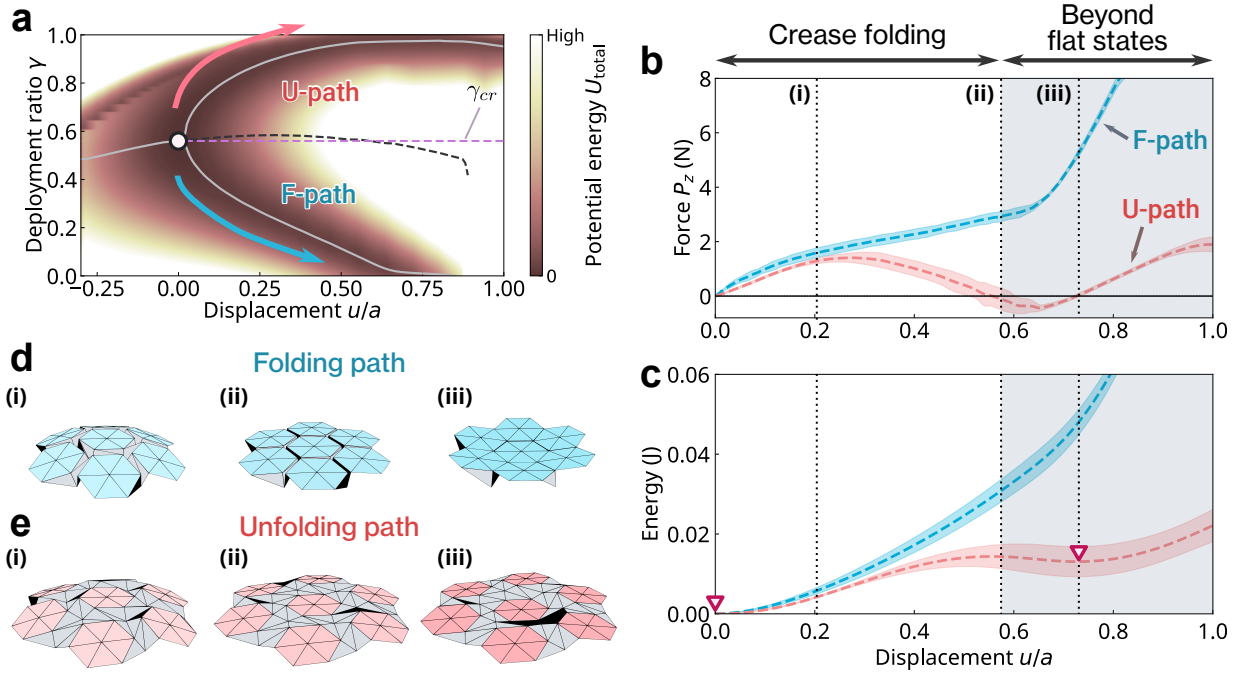


FIG. 2. **Static response under out-of-plane compression.** (a) Two deformation modes depicted as a bifurcation diagram. Light grey solid lines, stable branch; black dashed line, unstable branch. Violet dashed horizontal line denotes the γ_{cr} . (b) Force-displacement profile along the folding (red) and unfolding path (blue). (c) Potential energy landscape of the folding and unfolding cases shown in panel b, with local minima indicated by down-pointing triangles. Red dashed line, the folding path from experiment; blue dashed, the unfolding path from experiment. The shaded regions enclosing the dashed lines represent the standard deviation. The grey-shaded region beyond $u/a = 0.54$ implies the non-rigid foldable region. Folding postures are shown for (d) folding and (e) unfolding path.

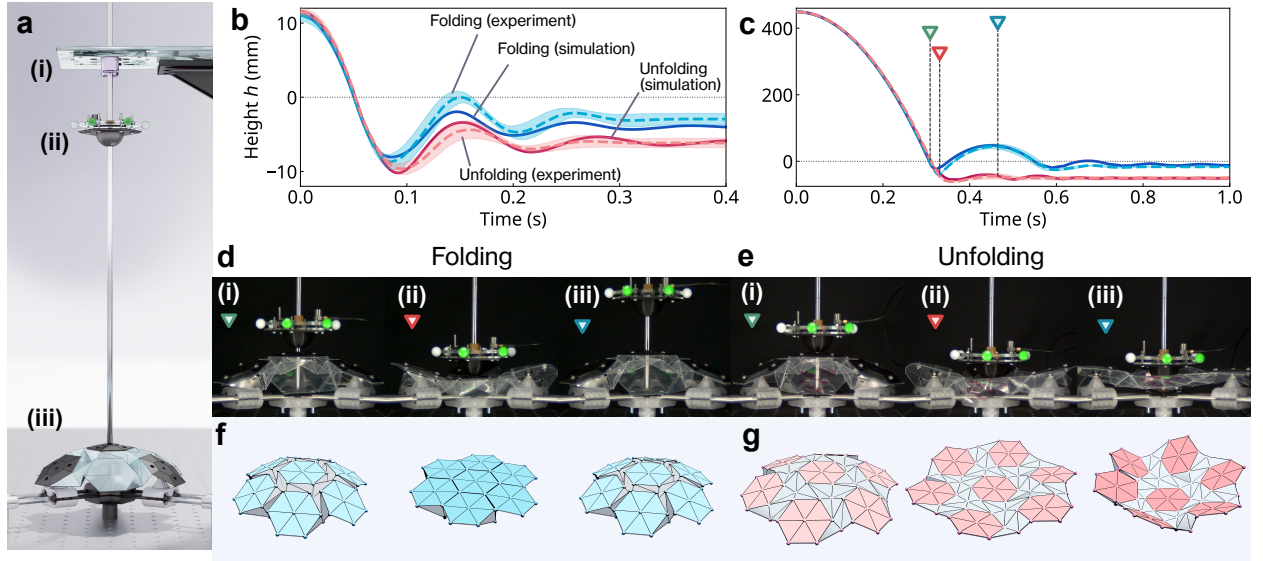


FIG. 3. **Impactor trajectory upon collision with Resch origami.** (a) Drop tower comprised of (i) electromagnet release system, (ii) impactor, and (iii) single-orbit Resch origami. Height of the impactor for the impact speed (b) 0.5 m/s, and (c) 3.0 m/s. Solid lines, simulation; dashed line, average of experimental data; shaded region; standard deviation of experimental data. Snapshot at (i) $t = 0.306$, (ii) 0.326, (iii) 0.455 s extracted from the experiment for (d) folding and (e) unfolding configuration. Snapshots of (f) folding and (g) unfolding configuration from simulation. Corresponding moments are marked in panel (c) with triangular symbols.

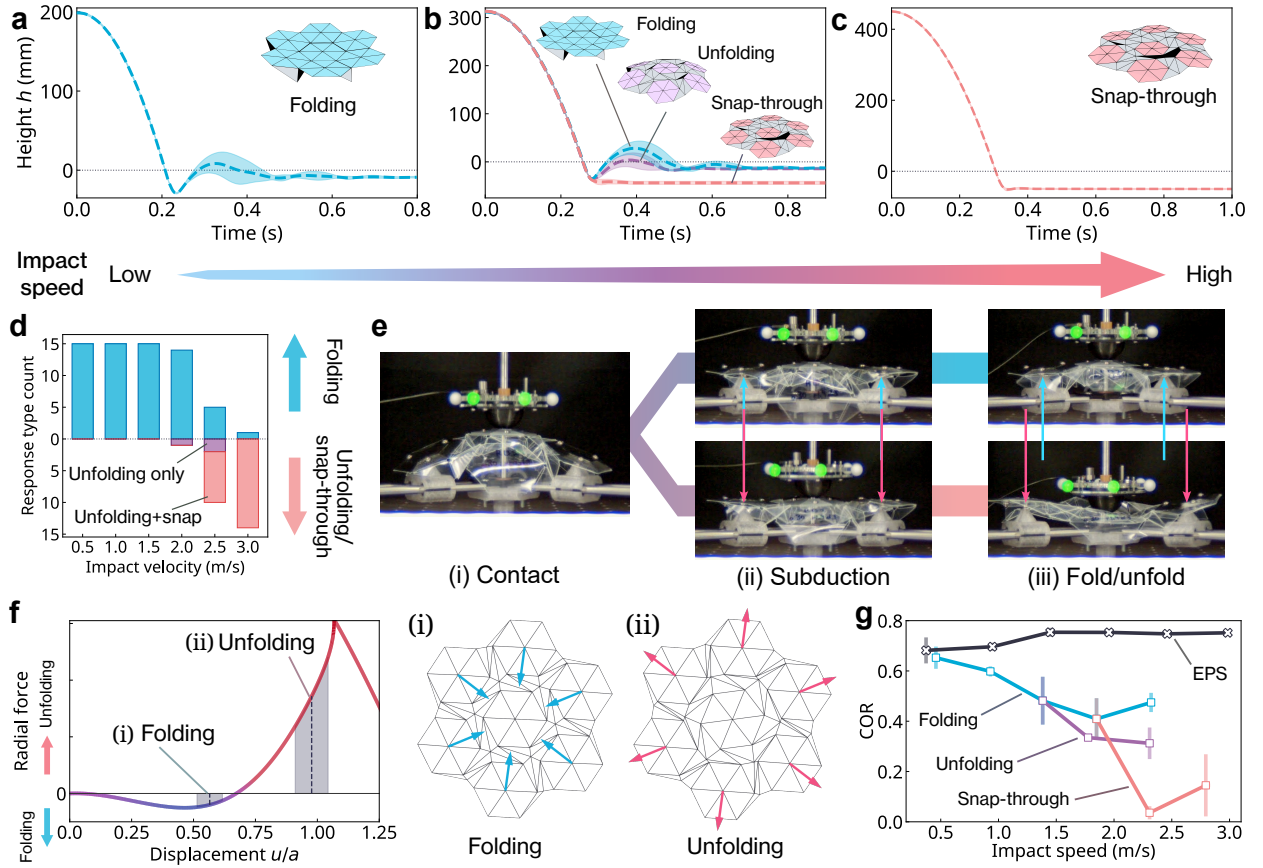


FIG. 4. **Dynamic bifurcation of Resch origami.** The height of the impactor for the case of (a) $v_{\text{impact}} = 2.0$ m/s, (b) 2.5 m/s, and (c) 3.0 m/s. The inset figures of each panel schematically display the folding mode that Resch origami follows. (d) Histogram of folding, unfolding, and snap-through as a function of impact speed. (e) Deformation sequence of the Resch origami, extracted from the experiment undergoing (i) contact, (ii) subduction, and (iii) fold/unfold phases. (f) Numerically estimated radial force exerted on the outer hexagons. Sub-panels correspond to the subduction displacement in (i) $v_{\text{impact}} = 2.0$ and (ii) 3.0 m/s cases. (g) Coefficient of restitution as a function of impact speed. Blue open-square symbol, folding mode; purple open-square symbol, unfolding mode; red open-square symbol, snap-through mode; grey cross symbol, EPS.

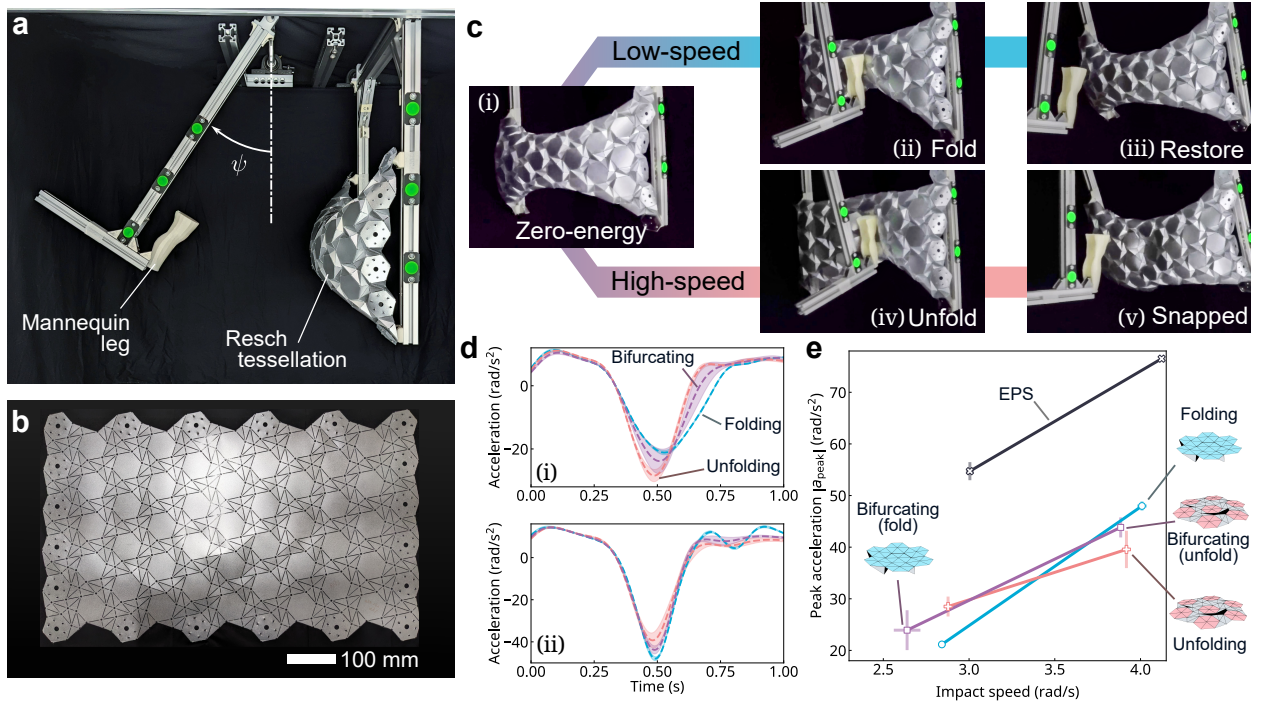


FIG. 5. **Meter-scale Resch-patterned impact mitigation system.** (a) Pendulum-based experimental set-up. (b) Laser-cut rectangular Resch-patterned origami tessellation. (c) Snapshot of Resch origami in bifurcating configuration. Release conditions are, $\psi_0 = 40.9^\circ$ for low impact speed and $\psi_0 = 57.8^\circ$ for high impact speed. (d) Acceleration of mannequin relative to Resch tessellation at (i) low-speed and (ii) high-speed impact case. Blue dashed lines, folding configuration case; purple dashed lines, bifurcating configuration case; red dashed lines, unfolding configuration case; (e) Peak acceleration. (f) Coefficient of restitution. Blue open circle symbol, folding configuration; purple open square symbol, bifurcating configuration; red open plus sign symbol, unfolding configuration; grey open X symbol, EPS.